Journal of the Meteorological Society of Japan

EARLY ONLINE RELEASE

The DOI for this manuscript is

DOI:10.2151/jmsj. 2018-007

J-STAGE Advance published date: December 8, 2017

The final manuscript after publication will replace the preliminary version at the above DOI once it is available.

Development of gas absorption tables and an atmospheric radiative transfer package for applications using the Advanced Himawari Imager

Miho SEKIGUCHI

Faculty of Marine Technology,
Tokyo University of Marine Science and Technology, Tokyo, Japan

Hironobu Iwabuchi

Graduate School of Science,
Tohoku University, Sendai, Japan

Takashi M. Nagao

Earth Observation Research Center,
Japan Aerospace Exploration Agency, Ibaraki, Japan

Teruyuki Nakajima

Earth Observation Research Center,
Japan Aerospace Exploration Agency, Ibaraki, Japan

Oct 5, 2017

Corresponding author: Miho Sekiguchi, Tokyo University of Marine Science and Technology, 2-1-6, Etchujima, Koto-ku, Tokyo 135-8533 Japan
Email: miho@kaiyodai.ac.jp
Tel: +81-3-5245-7463
Fax: +81-3-5245-7463

Abstract

We developed an atmospheric gas absorption table for the Advanced Himawari Imager (AHI) based on the correlated *k*-distribution (CKD) method with the optimization method, which was used to determine quadrature weights and abscissas. We incorporated the table and band information of the AHI into a multi-purpose atmospheric radiative transfer package, Rstar. We updated the package so that users could easily specify the satellite and band number. Use of this update made it possible for the optimized CKD method to carry out calculations rapidly and accurately. Rstar is easy for beginners to use and facilitates comparison of results. Cloud retrieval tests using different numbers of quadrature points showed that cloud retrievals could be significantly affected by the accuracy of the CKD model.

Keywords: satellite data analysis; atmospheric gas absorption; radiative transfer

1. Introduction

A radiative transfer code is fundamental to analysis of satellite observations. Several modern satellite remote sensing algorithms (Watts et al. 2011; Poulsen et al. 2012; Sourdeval et al. 2015, 2016) are being continuously developed using an optimal estimation method (Rodgers 2000). Iwabuchi et al. (2016, 2018) developed the Integrated Cloud

Analysis System (ICAS), which is an optimal estimation-based algorithm used to investigate global distributions of cloud properties. Hashimoto and Nakajima (2017) developed the Multi-Wavelength and multi-Pixel Method (MWPM), which is also based on an optimal estimation approach, to retrieve aerosol optical properties over heterogeneous surfaces. Although computational efficiency is not very important for making a look-up table (often used for analysis of satellite imager data), in these forward models, a radiative transfer code is needed to calculate radiative transfer rapidly and accurately many times and in many cases.

Several atmospheric radiative transfer codes have been developed for satellite analysis. For example, RTTOV (Radiative Transfer for TOVS) (Saunders et al. 1999) and 6S (Second Simulation of the Satellite Signal in the Solar Spectrum) (Vermote et al. 1997) are well known open access codes. In Japan, the authors manage the OpenCLASTR (Open Clustered Libraries for Atmospheric Science and Transfer of Radiation) project, from which packages and libraries for atmospheric radiation are developed and distributed. The STAR (System for Transfer of Atmospheric Radiation) series, which plays the main role in this project, contains RSTAR (Nakajima and Tanaka 1986, 1988) for radiance calculations, PSTAR (Ota et al. 2010) for polarized radiance calculations, FSTAR for radiative flux calculations, and MCSTAR (Okata et al. 2017) for three-dimensional Monte-Carlo calculations. RSTAR is a famous radiative transfer package introduced in several satellite retrieval algorithms. It was created in 1988 and has been continuously developed. The latest version is version 7.

However, some algorithms are incompatible with recent satellite sensors. The developmental policy of RSTAR is to provide a package that is general and versatile, but such a package requires complicated and detailed specifications for a particular purpose. For a satellite analysis, users have to set the wavelength at the band center, the bandwidth, and the spectral response function of the band that the user wants to analyze. It may be difficult for beginners to specify these settings appropriately to facilitate comparing results with different settings, and it is time-consuming to perform calculations many times with a single setting (i.e., the same set of values for many parameters). Most radiative transfer codes for satellite analyses already include information about sensors; users indicate only the index numbers of the band and sensor as input data. For example, 6S, a radiative transfer code for clear sky and the solar wavelength region, contains spectral response functions at a resolution of 0.025 μm and calculates radiative quantities by using an approximation method that involves successive orders of scattering at each wavelength. Rstar uses the discrete-ordinate method for radiative transfer and can treat particle scattering accurately, but it takes a relatively long time to achieve the same resolution as 6S.

The Himawari-8 satellite carries the Advanced Himawari Imager (AHI), the resolution of which is greatly improved both spatially and temporally compared to previous meteorological satellites of Japan, GMS and MTSAT series (Bessho et al. 2016). Figure 1 shows the spectral distribution of the outgoing radiance at the top of the atmosphere (TOA) and the surface of Earth multiplied by the response function within the wavelength range of the AHI band #16. The satellite zenith angle was assumed to be 0°. Atmospheric conditions were assumed to be typical of an Air Force Geophysics Laboratory (AFGL) standard atmosphere at mid-latitudes during the summer (Anderson et al. 1986), but the CO_2 concentration was assumed to be 360 ppm. This spectral response function is a transmittance which is provided by Meteorological Satellite Center of Japan Meteorological Agency (JMA), spectrally integrated value of Fig. 1 is equal to satellite-observed radiance in the atmospheric condition as described above. To integrate such a spiky spectral distribution, a large number of quadrature abscissas are needed.

The correlated *k*-distribution (CKD) method (Lacis and Oinas 1991; Fu and Liou 1992) is a rapid method to evaluate atmospheric gas absorption, and it has been incorporated into many broadband models. In this study, we used this method for each wavelength band of the sensors to increase the efficiency of gas absorption process. Moreover, by adopting an optimization method to determine quadrature abscissas and weights, we reduced the number of radiative transfer calculations. Furthermore, we introduced an optimization method into Rstar, and we updated the package of Rstar so that it was suitable for satellite retrieval analysis. Section 2 describes the models and datasets that we used. In Section 3, the optimized CKD method and it's evaluations are explained. Section 4 shows the results retrieved by the AHI with this method. Section 5 summarizes this paper.

2. Models and Datasets

Rstar7 is a narrow-band model that contains two standard gas absorption tables. It covers the wavenumber spectrum from 10 to 54,000 cm^{-1}, a range that it divides log-linearly into 3732 or 7464 bands. The bandwidths in units of the base-10 logarithm of the wavenumber are 0.001 and 0.0005. For this reason, the bandwidths tend to be wider at shorter wavelengths. These bandwidths may be incompatible with the resolution of the AHI. When the CKD method is applied, the number of quadrature points is fixed at two per band. The abscissas and weights for integration are determined by squared Gaussian quadrature whose abscissas are doubled abscissas of Gaussian quadrature and weights are products of abscissas and weights of that. Perfectly correlated overlapping is assumed in a band where multiple gases are involved. The absorption coefficients of the seven major gases (H_2O, CO_2, O_3, N_2O, CO, CH_4, and O_2) in each band are tabulated for 26 log-linear levels of pressure and 3 levels of temperature. The atmospheric gas absorption database HITRAN 2004 (Rothman et al. 2005) is used for line absorptions, and MT_CKD_1 code (Mlawer et al. 2012) is used for continuous absorption. As discussed above, users set quadrature points and weights for spectral integration by Rstar.

To make calculations rapid and accurate, we created a new gas absorption table corresponding to each AHI band. We applied the CKD method, and we reduced the number of quadrature points by using an optimization method to determine the abscissas and weights for integration. This method combining the CKD and optimization was originally developed for MSTRNX (Model Simulation radiation TRaNsfer code) (Sekiguchi and

Nakajima 2008, hereafter called SN08 in the text), which is a broadband model adapted to MIROC (Model for Interdisciplinary Research on Climate) (Watanabe et al. 2010) and NICAM (Nonhydrostatic Icosahedral Atmospheric Model) (Satoh et al. 2008) and is known to be a fast and stable radiative transfer code. We used HITRAN 2012 (Rothman et al. 2013), the latest version of HITRAN and MT_CKD_2.1, to obtain absorption coefficients. The MT_CKD_2.1 code, which we used to calculate continuous absorption spectra, was developed by AER Inc. and was updated to version 3, which corresponds to HITRAN 2012. We plan to continue updating with the latest version.

3. Methods

The optical characteristics of particle scattering, solar irradiance, and the Planck function for blackbody radiation should be independent of wavelength within a band when the CKD method is used for each band. However, in two AHI bands, optical properties vary significantly with wavelength. In AHI band 3, absorption by oxygen is present in part of the spectrum but weak in other parts. AHI band 8 is very wide compared to the other bands, and within band 8 the Planck function varies greatly with wavelength. We divided these two bands into two sub-bands. We initially specified the bandwidths and the gases in each band of the AHI as indicated in Table 1. In this study, the bandwidths are defined the full width at half maximum (FWHM) of the spectral response function (SRF) and we applied the CKD method to each bandwidth. To determine the important absorption gases in each band, we compared calculated radiative fluxes with or without a target gas by reference calculations, whose resolutions were same as that of SRF distributed by JMA; they were 0.1 cm^{-1} (band #7 to #16) or 1.0 cm^{-1} (band #1 to #6), respectively. We took a target gas into consideration if the error due to neglect of that gas was larger than 1%. We sorted the spectral absorption coefficients within each bandwidth to generate a *k*-distribution. We stored the *k*-distributions of the target gas species at 26 pressure levels from 0.01 to 1013.25 hPa and three temperatures (200, 260, and 320 K) for each band.

A trapezoidal or Gaussian quadrature is often used to carry out numerical integrations in the *k*-distribution method. In this study, however, we determined the quadrature abscissas and weights using sequential quadratic programming, which is an interactive method for nonlinear optimization. This method is almost same as SN08, but different in two points. One is the setting of the objective function, and the other is the way to select appropriate quadrature abscissas and weights.

In this optimization process, quadrature abscissas and weights were set so as to minimize an objective function. The objective function was defined as the square root of the sum of the squared differences between calculations with this method and reference results of the radiative fluxes at the TOA and surface and profiles of heating rates. This setting of the objective function is same as SN08 but Line-By-Line method were used as a reference calculation in SN08. The reference results are calculated radiative fluxes and heating rate with high-spectral resolution, multiplied by the spectral response function and integrated over a bandwidth. The spectral resolutions of the reference calculation were set as same as the SRF. We used six AFGL standard atmospheric conditions (but CO_2 concentrations were modified to 360 ppm) in these calculations. We assumed clear sky conditions because scattering by clouds and aerosols impacted the reference results and made the optimization difficult. To take into account variations of optical path lengths due to multiple scattering and differences in the positions of the sun and satellite, we assumed optical path lengths that satellite zenith angles were equivalent to either 0° or 60°. This setting is also different from SN08.

When the objective function decreased, the optimization had sometimes identified a local rather than global minimum. To avoid this problem, we started the optimization process from two initial conditions if the band included more than two gas species. One was a completely correlated overlapping, and the other was a completely uncorrelated overlapping. The initial abscissas and weights were calculated by Gaussian quadrature. Subsequently, we used two processes to change the number of quadrature points, N_c. One process was to optimize for each N_c separately, and the other was to decrease N_c sequentially. In the latter case, the optimization process started from N_c = 8 (the initial condition corresponded to completely correlated overlapping, or the number of gas species was 1 or 3 if the initial condition corresponded to completely uncorrelated overlapping) or 9 (the number of gas species was 2 if the initial condition corresponded to completely uncorrelated overlapping). When the optimization process with N_c quadrature points was completed, the initial condition corresponding to N_c – 1 quadrature points was defined, and the quadrature point that contributed the least was removed from the optimized quadrature with N_c quadrature points. With this method, we were able to obtain optimized results in each case of N_c quadrature points. We selected the set of abscissas and weights that gave the best results. Finally, the CKD parameters were determined for N_c from 1 to 6. In SN08, N_c is not selectable and already set to perform properly with all band in GCM, on the other hand, in this study, users could select the N_c best suited for their purposes.

Figure 2 shows the differences of radiative fluxes that were calculated with the optimized CKD method for N_c = 1, 2, 4, and 6 from the reference calculation. Panels corresponding to Visible (VIS) – Near InfraRed (NIR) bands (bands #1–#7) show net flux differences, and panels corresponding to Thermal InfraRed (TIR) bands (bands #8–#16) show upward flux differences. Atmospheric conditions were assumed to correspond to those of the mid-latitude summer model of the AFGL standard atmosphere. The solar zenith angle was assumed to be 60° and the surface was to be Lambertian with an albedo 0.1 in VIS-NIR bands, surface emissivity was assumed 1.0 in TIR bands. In bands #3 and #8, which were divided into two sub-parts, the same N_c was used in each sub-part, and the results were summed. The satellite received radiances are observed at TOA, however, the profile of radiance is important for cloudy sky cases. In general, the larger the value N_c, the better the results. In the case of bands treated a single gas species, the difference from the reference was smaller than in the case of multiple gases (see also Table 1) because the optimization process converged easily. The altitude of the maximum difference would indicate a maximum dependency of a main target gas in each band. We also checked angular dependencies of satellite received radiance. The differences between results by the combined CKD method and the reference method were not changed with satellite zenith angle in TIR bands, but in VIS-NIR bands, the differences became large in larger satellite zenith angles, their variance is about same as the method difference. We plan to increase satellite zenith angles of the objective functions in next update.

4. Calculation check

We used the CKD table corresponding to $N_c = 6$ in the forward model of the ICAS (Iwabuchi et al., 2018) to simulate brightness temperatures in eight TIR bands (bands #9–#16) for clear sky pixels over the ocean observed by the AHI. In the calculations, the land and ocean surface temperature and emissivity were obtained from the moderate resolution imaging spectroradiometer (MODIS) 8-day mean land and ocean products, and the atmospheric profiles of temperature and concentrations of water vapor and ozone were interpolated spatially and temporally from the Modern-Era Retrospective analysis for Research and Applications (MERRA) meteorological field product (Rienecker et al. 2011). Concentrations of CO_2, N_2O, and CH_4 were assumed to be equal to monthly mean values of global mean. The forward model is based on the two-stream solution of radiative transfer in the plane-parallel multilayered atmosphere. Details of error evaluation for the AHI longwave bands are presented in Iwabuchi et al. (2018). Figure 3 shows scatter plots between the observed and model-simulated brightness temperature for each AHI band. We used full disk data for the period 19–28 August 2015. Discrimination of clear sky pixels was based on confidently clear sky pixels identified by the collocated moderate resolution imaging spectroradiometer (MODIS) cloud mask product. The means and standard deviations of the differences between model simulations are shown in Table 2. We attribute these differences to errors in the assumed temperatures and water vapor profiles, sea surface temperatures (SST), and the gas absorption table calculated with the optimized CKD method. The standard deviation of the SST error was estimated to be about 0.4–0.5 K and the radiometric calibration accuracy ranged from 0.20–0.29 %, which was converted to 0.11–0.18 K when brightness temperature was assumed 300K. Given this estimated standard deviation, the trends of the model results and observations were in good agreement, except for band #11, for which the model results were overestimates. One of the reasons may be that SO_2 was not considered in that band of this version, whereas the other three gas species (H_2O, N_2O, and CH_4) were taken into consideration (Table 1). The transmittance which is considered SO_2 in this band is estimated about 90.2 % with AFGL concentration profile of SO_2, on the other hand, that which is not considered is estimated about 90.7 %. SO_2 is considered one of main gas species in this band and the target of this band in the AHI design, it should be included in the gas absorption model and will be introduced in next update. In the water vapor bands (bands #9 and #10), the standard deviation of the error was larger than 1 K. These figures are used in clear sky pixels over the ocean, the error sources are limited for the error of atmospheric gas profiles and SST. Because these bands are sensitive to the atmospheric profiles in the middle and upper troposphere, SST error is not estimated for the main reason in these band. Compared to temperatures, water vapor amounts in the middle and upper troposphere in the atmospheric reanalysis product are considered to be more uncertain. A main source of uncertainty in these bands is considered the error of the assumed amounts of water vapor in the middle and upper troposphere. For the VIS-NIR bands, we considered a similar analysis that uses the TOA reflectance (not shown), but we needed more information such as aerosol optical properties and sea surface emissivity. That analysis is therefore left for a future study.

Infrared measurements for cloudy pixels are sensitive mainly to cloud top temperature, cloud optical thickness, and particle effective radius and secondly to cloud geometrical thickness and vertical inhomogeneity in addition to surface properties and atmospheric profile. Not all of the cloud parameters are available very reliably from observation data. To evaluate the CKD models, however, it would be interesting to test model–measurement consistency and impact of CKD model on cloud retrieval. Cloud properties were retrieved using the ICAS, in which different values of N_c as 2, 3, and 6 were used for forward calculations of brightness temperatures. A set of retrieved cloud properties and simulated brightness temperatures were obtained for optimal solutions. The optimal estimation framework used in ICAS attempts to estimate cloud properties that best fit to the measurements. Thus, the model calculations should fit well to the measurements if the forward model has smaller errors, and vice versa. Figure 4 shows histograms of brightness temperature differences between model calculations and measurements for the cloud retrieval results. The mean difference between the measurements and model with N_c = 2 was different from zero, whereas the mean bias with N_c = 6 was almost zero except for band #12. In band #12, the means of the BT difference was larger with larger N_c, however, the shape of histogram was more symmetric with larger N_c. The mean biases were generally smaller than the clear sky cases shown in Fig. 3 because the model calculations were fitted to the measurements in the optimal estimation-based cloud property inversion. In the water vapor bands (bands #9 and #10), standard deviations of the differences were larger than those in the other bands. The reason was the same as in the clear sky cases. The standard deviations of the differences for N_c = 2 were significantly larger than those for N_c = 3 and 6, the indication being that the model that uses N_c = 2 did not fit the measurements well.

The global distributions of cloud top height (CTH) and cloud optical thickness (COT) retrieved by using the optimized CKD table with different numbers of quadrature points (N_c = 2, 3, and 6) are shown in Fig. 5. These results are shown only for pixels with solutions optimized via the ICAS. The number of pixels was significantly smaller for N_c = 2 than for N_c = 3 and 6, and the spatial distributions of cloud properties retrieved with N_c = 3 and 6 seemed reasonable. The differences in COT and CTH as a function of N_c are shown quantitatively in Fig. 6. Although a difference between N_c = 3 and 6 was not clearly apparent in Fig. 5, a difference of COT for low clouds is apparent in Fig. 6b. Comparing only pixels with optimal solutions, high-cloud COT was estimated better than low-cloud COT, irrespective of N_c. Because the ICAS uses eight thermal infrared bands of the AHI, the estimation of COT can be more certain for high clouds than low cloud because of larger difference between cloud and underlying-surface temperatures. The difference between N_c = 2 and 6 was widely distributed (Figs. 6a and 6c), which is primarily due to misinterpretation of low cloud as high cloud in the retrieval with N_c = 2. This misinterpretation is found over the Indian Ocean near the western coast of Australia, as shown in Fig. 5. Because brightness temperatures are generally comparable for optically thick low cloud and optically thin high cloud, it is an inter-band consistency (i.e. brightness temperature differences among bands) to discriminate the two types of cloud. It is suggested that inter-band consistency is not very good for N_c = 2.

Calculations by the modified Rstar package were rapid. Figure 7 shows an example of cloud retrieval fields over the Sea of Japan at 01 UTC and 04 UTC on 7 April 2017 that used the satellite analysis version of Rstar developed in this study. Cirrus clouds were present in the upper left of the images at 01 UTC, and low clouds were located in the center of the same images. The cirrus and low clouds overlapped at 04 UTC. The top, second, third, and bottom panels show true-color composite images, COT retrieval results, cloud effective radii (CER), and CTHs, respectively. The panels on the left were retrieved using VIS, NIR, and TIR bands (bands #4, #6, and #13, respectively). The panels on the right were retrieved using TIR bands (bands #11, #13, and #15). Compared with two results of CERs and CTHs at overlapping pixels, it is apparent that the VIS-NIR-TIR method retrieves mainly low clouds, whereas the TIR method retrieves mainly parameters of cirrus clouds. The various bands of the AHI provide much information about many targets, the modified Rstar package would work for high-resolution satellite analysis.

5. Summary

We developed gas absorption tables by using an optimized CKD method for rapid and accurate simulations of satellite measurements. The number of quadrature points, N_c, directly affected computational efficiency. We made CKD parameter tables in which N_c varied from 1 to 6 and could be selected by the user. We have checked cloud retrieval results with different values of N_c. In cases with $N_c = 2$, cloud retrieval results were significantly different from those with $N_c > 2$. We recommend $N_c > 3$ for high accuracy.

In this study, we used radiative flux and heating rate for the objective function as same as SN08, however, it is suitable for satellite analysis to use radiance in various solar and satellite angles and surface condition. In addition, we considered difficult to adopt cloud and aerosol for the objective function, because it is needed to divide error sources from gas absorption and particle scattering and the objective function is not easy to converge if the number of parameters increases. We plan to study effects of several parameters for the objective function. We also plan to update the latest version of continuum program MT_CKD_3, and introduce SO_2 absorptions in band 10 and 11. The spectral responsivity of AHI-9 mounted on Himawari-9 is slightly different from AHI-8, the extension to AHI-9 is also planned.

We incorporated the CKD tables and band information of the AHI into a multi-purpose atmospheric radiative transfer package, Rstar. We updated the package for satellite analysis so that the user could easily specify the satellite and band number. We also developed tables for Aqua/MODIS, CALIPSO/IIR, and Landsat-7/ETM+. This package makes possible cloud and aerosol retrievals with high speed and high precision that are suitable for high-frequency and high-resolution observations made by satellites such as Himawari-8.

Acknowledgments

This research was supported by the Earth Observation Priority Research of the Japan Aerospace Exploration Agency (JAXA) (JX-PSPC-443963). Miho Sekiguchi and Hironobu Iwabuchi acknowledge the support of the First Research Announcement on the Earth Observations of JAXA (PI No.: RA1R502 and RA1R306).

References

Anderson, G. P., S.A. Clough, F.X. Kneizys, J.H. Chetwynd, and E.P. Shettle, 1986: AFGL atmospheric constituent profiles (0.120 km), Air Force Geophysics Lab, United States of America, 48pp.

Bessho, K., K. Date, M. Hayashi, A. Ikeda, T. Imai, H. Inoue, Y. Kumagai, T. Miyakawa, H.

Murata, T. Ohno, A. Okuyama, R. Oyama, Y. Sasaki, Y. Shimazu, K. Shimoji, Y. Sumida, M. Suzuki, H. Taniguchi, H. Tsuchiyama, D. Uesawa, H. Yokota, and R. Yoshida, 2016: An introduction to Himawari-8/9 — Japan's new-generation geostationary meteorological satellites, *J. Meteor. Soc. Japan*, **94**, 151–183.

Fu, Q., K.N. Liou, 1992: On the correlated *k*-distribution method for radiative transfer in nonhomogeneous atmospheres, *J. Atmos. Sci.,* **49**, 2139–56.

Iwabuchi, H., M. Saito, Y. Tokoro, N. S. Putri, and M. Sekiguchi, 2016: Retrieval of radiative and microphysical properties of cloud from multispectral infrared measurements, *Progress Earth Planet. Sci.,* **3,** 32, doi:10.1186/s40645-016-0108-3.

Iwabuchi, H., N. S. Putri, M. Saito, Y. Tokoro, M. Sekiguchi, P. Yang, and B. A. Baum, 2018: Cloud property retrieval from multiband infrared measurements by Himawari-8. *J. Meteor. Soc. Japan*, **96B**, http://doi.org/10.2151/jmsj.2018-001.

Hashimoto, M., and T. Nakajima, 2017: Development of a remote sensing algorithm to retrieve atmospheric aerosol properties using multi-wavelength and multi-pixel information. *J. Geophys. Res. Atmos.,* **122**, 6347–6378, doi:10.1002/2016JD025698.

Lacis, A.A. and V.A. Oinas 1991: Description if the correlated *k*-distribution method for modeling nongray gaseous absorption, thermal emission, and multiple scattering in vertically inhomogeneous atmospheres., *J. Geophys. Res*. **96**, 9027–63.

Mlawer, E.J., V.H. Payne, J.L. Moncet, J.S. Delamere, M.J. Alvarado, D.D. Tobin, 2012: Development and recent evaluation of the MT_CKD model of continuum absorption., *Phil.*

Trans. R. Soc. A., **37,** 1–37, doi:10.1098/rsta.2011.0295.

Nakajima, T., and M. Tanaka, 1986: Matrix formulations for the transfer of solar radiation in a plane-parallel scattering atmosphere, *J. Quant. Spectrosc. Radiat. Transfer*, **35**, 13–21.

Nakajima, T., and M. Tanaka, 1988: Algorithms for radiative intensity calculations in moderately thick atmospheres using a truncation approximation, *J. Quant. Spectrosc. Radiat. Transfer*, **40**, 51-69.

Okata, M., T. Nakajima, K. Suzuki, T. Inoue, T.Y. Nakajima, and H. Okamoto, 2017: A study on radiative transfer effects in 3D cloudy atmosphere using satellite data, *J. Geophys. Res*., 122(1), 443-468. doi:10.1002/2016JD025441.

Ota, Y., A. Higurashi, T. Nakajima, and T. Yokota, 2010: Matrix formulations of radiative transfer including the polarization effect in a coupled atmosphere–ocean system, *J. Quant. Spectrosc. Radiat. Transfer*, **111**, 878–894, doi:10.1016/j.jqsrt.2009.11.021

Poulsen, C. A., R. Siddans, G. E. Thomas, A. M. Sayer, R. G. Grainger, E. Campmany, S. M. Dean, C. Arnold, and P. D. Watts, 2012: Cloud retrievals from satellite data using optimal estimation: evaluation and application to ATSR, *Atmos. Meas. Tech*., **5**, 1889–1910.

Rienecker, M. M., M. J. Suarez, R. Gelaro, R. Toding, J. Bacmeister, E. Liu, M. G. Bosilovich, S. D. Schubert, L. Takacs, G. K. Kim, S. Bloom, J. Chen, D. Collins, A. Conaty, A. Silva, W. Gu, J. Joiner, R. D. Koster, R. Lucchesi, A. Molod, T. Owens, S. Pawson, P. Pegion, C. R. Redder, R. Reichle, F. R. Robertson, A. G. Ruddick, M. Sienkiewicz, and J. Woollen, 2011: MERRA: NASA's modern-era retrospective analysis for research and applications, *J. Clim.* **24**, 3624–3648.

Rodgers, C. D., 2000: *Inverse Methods for Atmospheric Sounding: Theory and Practice,* World Scientific, Singapore, 238 pp.

Rothman, L.S., D. Jacquemart, A. Barbe, D.C. Benner, M. Birk, L.R. Brown, M.R. Carleer, C. Chackerian Jr., K. Chance, L.H. Coudert, V. Dana, V.M. Devi, J.-M. Flaud, R.R. Gamache, A. Goldman, J.-M. Hartmann, K.W. Jucks, A.G. Maki, J.-Y. Mandin, S.T. Massie, J. Orphal, A. Perrin, C.P. Rinsland, M.A.H. Smith, J. Tennyson, R.N. Tolchenov, R.A. Toth, J. Vander Auwera, P. Varanasi and G. Wagner, 2005: The HITRAN 2004 molecular spectroscopic database, *J. Quant. Spectrosc. Radiat. Transfer*, ***96***(2), 139-204.

Rothman, L.S., I.E. Gordon, Y. Babikov, A. Barbe, D.C. Benner, P.F. Bernath, M. Birk, L. Bizzocchi, V. Boudon, L.R. Brown, A. Campargue, K. Chance, E.A. Cohen, L.H. Coudert, V.M. Devi, B.J. Drouin, A. Fayt, J.M. Flaud, R.R. Gamache, J.J. Harrison, J.M. Hartmann, C. Hill, J.T. Hodges, D. Jacquemar, A. Jolly, J. Lamouroux, R.J. Le Roy, G. Li, D.A. Long, O.M. Lyulin, C.J. Mackie, S.T. Massie, S. Mikhailenko, H.S.P. Müller, O.V. Naumenko, A.V. Nikitin, J. Orphal, V. Perevalov, A. Perrin, E.R. Polovtseva, C. Richard, M.A.H. Smith, E. Starikova, K. Sung, S. Tashkun, J. Tennyson J, G.C. Toon, V.I.G. Tyuterev, G. Wagner, 2013: The HITRAN2012 molecular spectroscopic database, *J. Quant. Spectrosc. Radiat. Transfer*, **130**, 4-50.

Satoh, M., T. Matsuno, H. Tomita, H. Miura, T. Nasuno and S. Iga, 2008: Nonhydrostatic

Icosahedral Atmospheric Model (NICAM) for global cloud resolving simulations. *J. Comput. Phys.*, **227**, 3486-3514, doi:10.1016/j.jcp.2007.02.006.

Saunders, R., M. Matricardi, and P. Brunel, 1999: An improved fast radiative transfer model for assimilation of satellite radiance observations, *Quart. J. Roy. Meteor. Soc.*, **125**, 1407-1425.

Sekiguchi, M., and T. Nakajima, 2008: A *k*-distribution-based radiation code and its computational optimization for an atmospheric general circulation model, *J. Quant. Spectrosc. Radiat. Transfer*, **109,** 2779–2793.

Sourdeval, O., L. C. Labonnote, A. J. Baran, and G. Brogniez, 2015: A methodology for simultaneous retrieval of ice and liquid water cloud properties. Part 1: Information content and case study, *Quart. J. Roy. Meteor. Soc.*, **141,** 870–882.

Sourdeval, O., L. C. Labonnote, A. J. Baran, J. Mülmenstädt, and G. Brogniez, 2016: A methodology for simultaneous retrieval of ice and liquid water cloud properties. Part 2: Near-global retrievals and evaluation against A-Train products, *Quart. J. Roy. Meteor. Soc.*, **142,** 3063–3081.

Vermote, E.F., D. Tanré, J.L. Deuzé, M. Herman and J.-J. Morcrette, 1997: Second Simulation of the Satellite Signal in the Solar Spectrum, 6S: An Overview, *IEEE Transactions on Geoscience and Remote Sensing*, **35**, 3, 675-686.

Watanabe, M., T. Suzuki, R. O'ishi, Y. Komuro, S. Watanabe, S. Emori, T. Takemura, M. Chikira, T. Ogura, M. Sekiguchi, K. Takata, D. Yamazaki, T. Yokohata, T. Nozawa, H.

Hasumi, H. Tatebe, and M. Kimoto, 2010: Improved climate simulation by MIROC5: Mean states, variability, and climate sensitivity, *J. Clim.*, **23**, 6312-6335.

Watts, P. D., R. Bennartz, and F. Fell, 2011: Retrieval of two-layer cloud properties from multispectral observations using optimal estimation, *J. Geophys. Res.*, **116**, D16203, doi: 10.1029/2011JD015883.

List of Figures

Figure 1. Spectral distribution of the outgoing radiance multiplied by the response function at the TOA (solid line) and surface (broken line) for band #16. Atmospheric conditions were assumed to correspond to mid-latitude summer. The resolution of the wavenumber was 0.1 cm^{-1}.

Figure 2. Differences of radiative fluxes calculated by using the optimized CKD from the reference calculations. Solid, broken, dotted, and bold lines indicate results with N_c = 1, 2, 4, and 6, respectively. Panels corresponding to bands #1–7 show net flux differences, and panels corresponding to bands #8–16 show upward flux differences. Atmospheric conditions were assumed to be equal to those of the mid-latitude summer, AFGL standard atmosphere. The solar zenith angle was assumed to be 60°. In bands #3 and #8, which were divided into two sub-parts, the results for each N_c case were added.

Figure 3. Scatter plots of the observed and model-simulated brightness temperatures for the TIR AHI band of clear sky pixels over the ocean. Full disk data for the period 19–28 August 2015 were used. Discrimination of clear sky pixels was based on confidently clear-sky pixels in the MODIS cloud mask product. Red lines denote fits and black diagonal lines indicate the identity. Means and standard deviations of the differences (observed minus modeled) are summarized in Table 2.

Figure 4. Histograms of the brightness temperature (BT) differences between measurements and model calculations for the cloud retrieval results for full disk data of

12 UTC on August 20, 2015. Cloud retrieval was performed with CKD sets with different numbers of quadrature points (N_c). The means and standard deviations of the BT differences are shown in the legend in each panel.

Figure 5. Cloud optical thickness (COT) (a,b,c) and cloud top height (CTH) (d,e,f) retrieved by using CKD sets with different numbers of quadrature points (N_c) for full disk data at 12 UTC on 20 August 2015. Results are shown only for pixels with optimal solutions. (a,d) N_c = 6, (b,e) N_c = 3, and (c,f) N_c = 2.

Figure 6. Differences in (a,b) cloud optical thickness (COT) and (c,d) cloud top height (CTH) retrieved with CKD sets with different numbers of quadrature points. The vertical axes denote differences results with N_c = 2 (a,c) and N_c = 3 (b,d) from results with N_c = 6. The color shading denotes occurrence frequency. Results are shown only for optimal retrievals in both reduced (N_c = 2 or 3) and full (N_c = 6) sets.

Figure 7. Sample of low clouds and overlapping cirrus clouds over the Sea of Japan at 01 and 04 UTC on 7 April 2017. Top, second, third, and bottom panels are true-color composite images and retrieved results of COT, CER, and CTH, respectively. The panels on the left were retrieved using VIS, NIR, and TIR bands (bands #4, #6, and #13, respectively). The panels on the right were retrieved using TIR bands (bands #11, #13 and #15) with a version of Rstar that was updated for this study.

List of Tables

Table 1. Band number, center of band[μm], bandwidth[μm], and gases implemented in each band. Bandwidth is defined as the FWHM.

band number	**center wavelength [μm]**	**band width [μm]**	**gases implemented in band**
1	0.4703	0.0407	H_2O
2	0.5105	0.0308	H_2O
3-1	0.6090	0.0320	H_2O
3-2	0.6500	0.0500	H_2O, O_2
4	0.8563	0.0345	H_2O
5	1.6098	0.0409	H_2O
6	2.2570	0.0441	H_2O, CH_4
7	3.8848	0.2006	H_2O, CH_4
8-1	6.0387	0.4227	H_2O
8-2	6.4496	0.3993	H_2O
9	6.9395	0.4019	H_2O
10	7.3471	0.1871	H_2O, N_2O, CH_4
11	8.5905	0.3727	H_2O, N_2O, CH_4
12	9.6347	0.3779	H_2O, CO_2, O_3
13	10.403	0.4189	H_2O, CO_2
14	11.243	0.6678	H_2O, CO_2
15	12.383	0.9656	H_2O, CO_2, O_3
16	13.284	0.5638	H_2O, CO_2, O_3

Table 2. Mean differences [K] and standard deviations [K] of observed and model-simulated brightness temperatures for the TIR AHI bands of clear-sky pixels over the ocean (observed minus modeled). Scatter plots are shown in Fig. 3.

Band number	Mean difference	Standard deviation
9	0.50	1.61
10	0.39	1.14
11	–1.12	0.56
12	–0.26	0.63
13	–0.28	0.61
14	–0.51	0.71
15	0.03	0.75
16	0.19	0.56

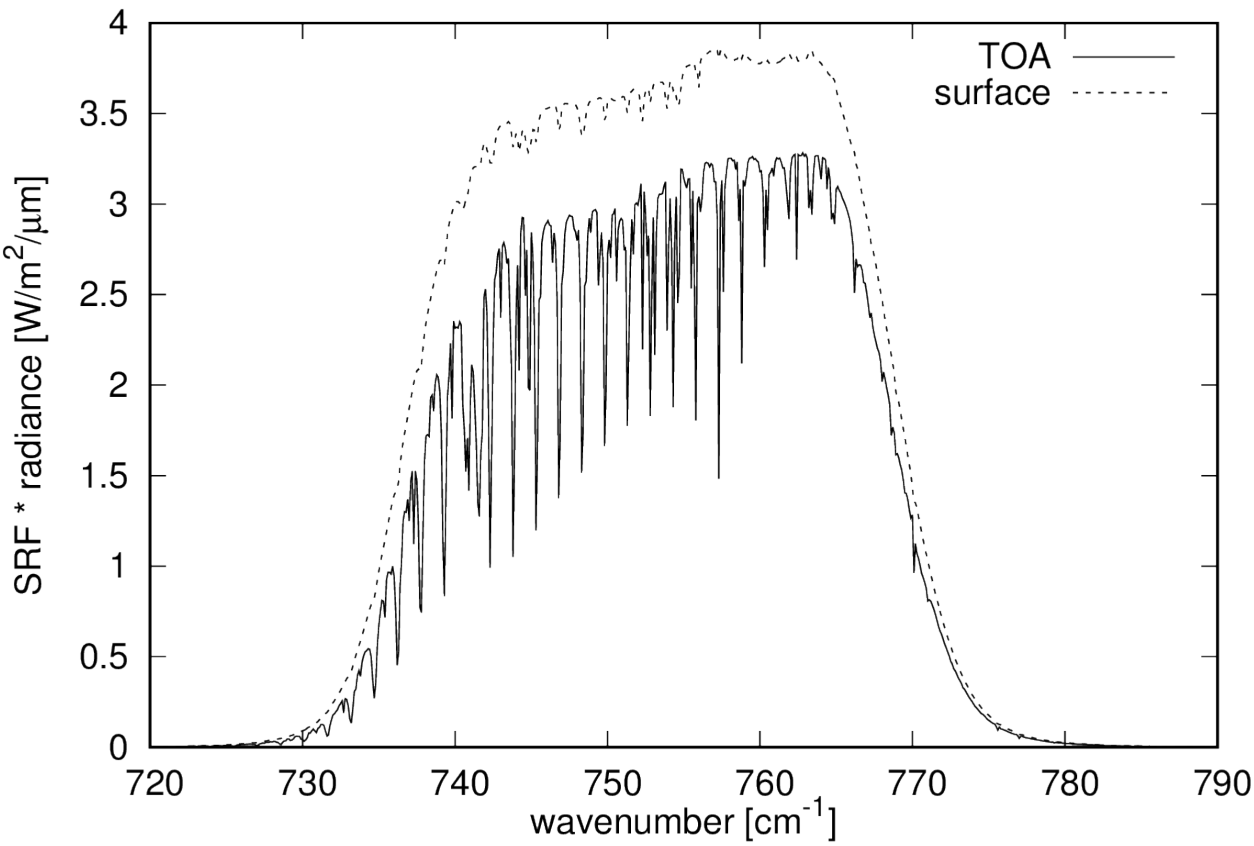

Fig. 1. Spectral distribution of the outgoing radiance multiplied by the response function at the TOA (solid line) and surface (broken line) for band #16. Atmospheric conditions were assumed to correspond to mid-latitude summer. The resolution of the wavenumber was 0.1 cm^{-1}.

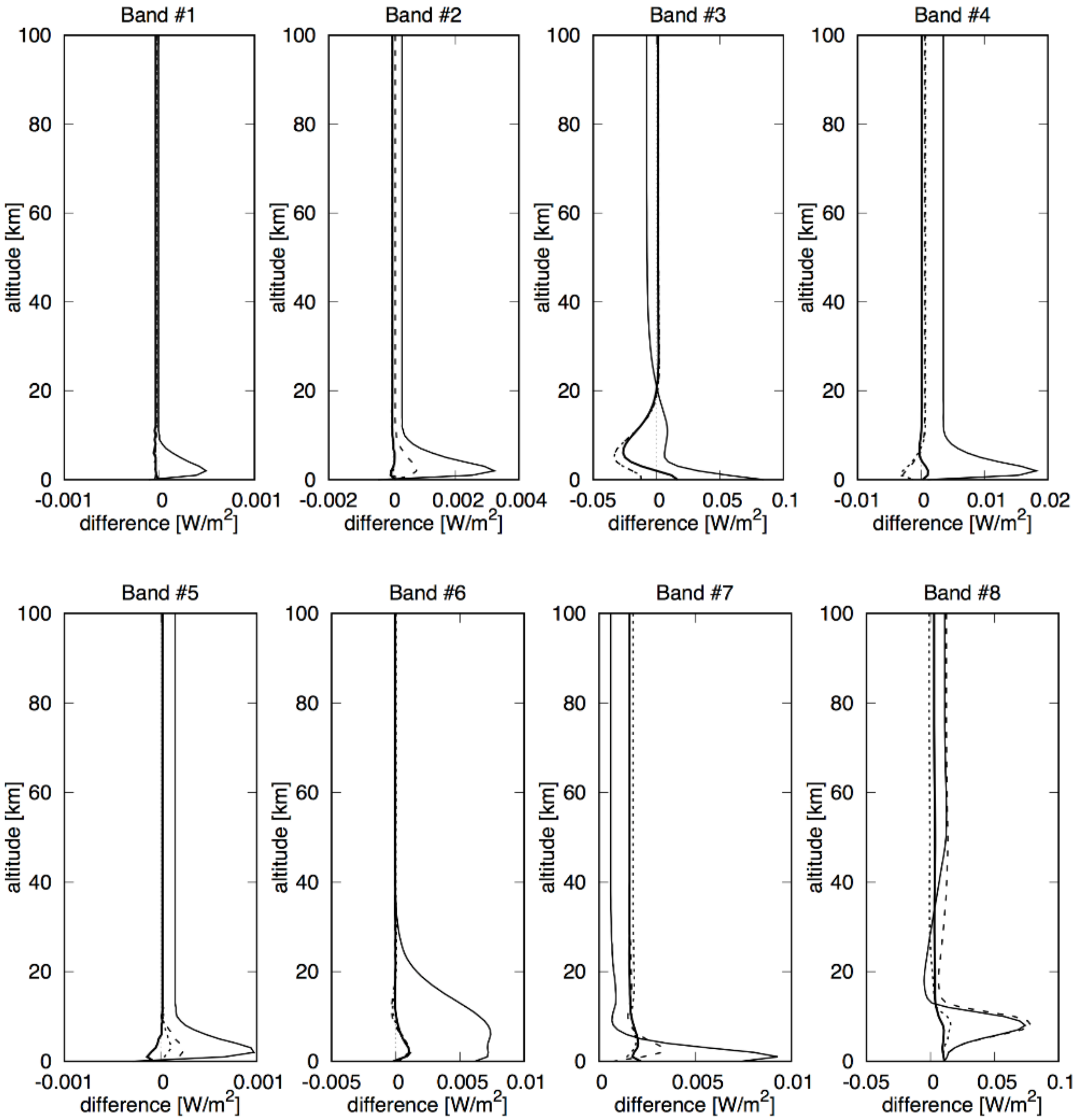

Band #1
Band #2
Band #3
Band #4
Band #5
Band #6
Band #7
Band #8
altitude [km]
difference [W/m^2]

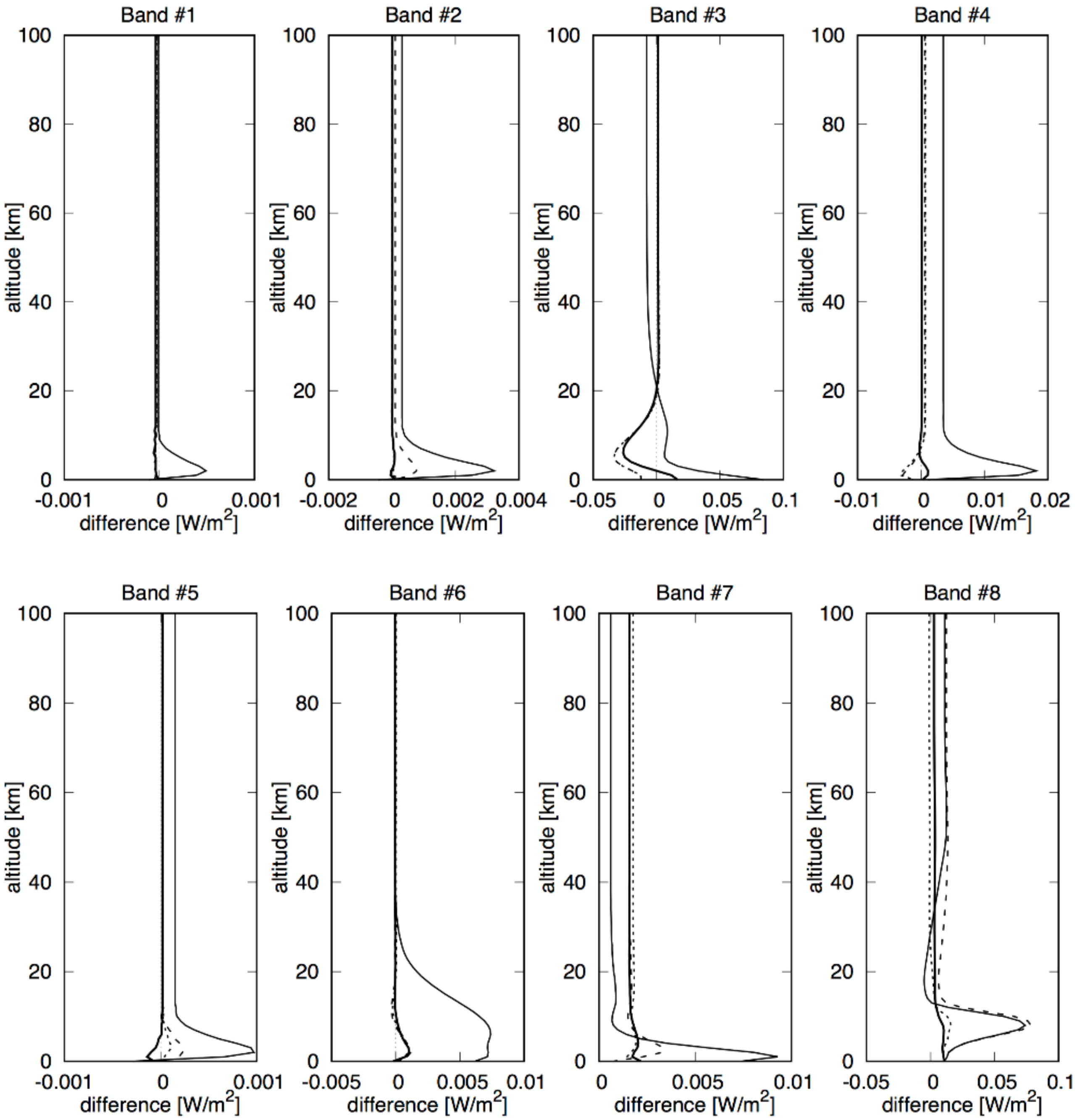

Band #1
Band #2
Band #3
Band #4
Band #5
Band #6
Band #7
Band #8
altitude [km]
difference [W/m2]
100
80
60
40
20
0
-0.001
0
0.001
-0.002
0.002
0.004
-0.05
0.05
0.1
-0.01
0.01
0.02
-0.005
0.005
0.01

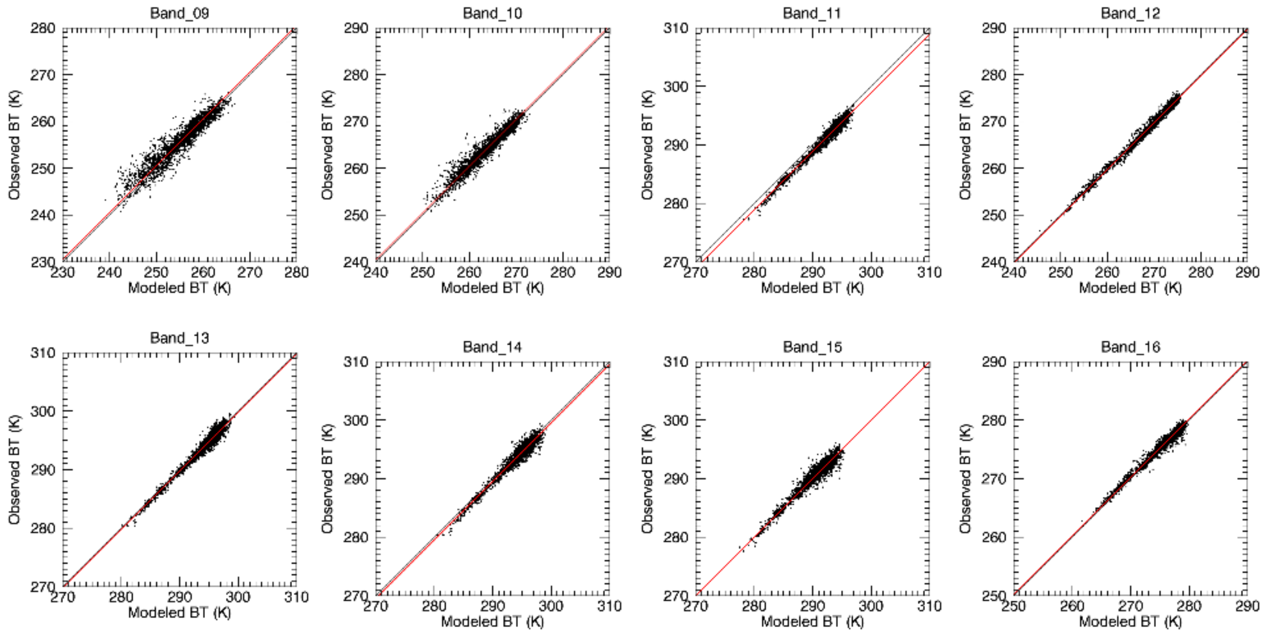

Fig. 3. Scatter plots of the observed and model-simulated brightness temperatures for the TIR AHI band of clear sky pixels over the ocean. Full disk data for the period 19–28 August 2015 were used. Discrimination of clear sky pixels was based on confidently clear-sky pixels in the MODIS cloud mask product. Red lines denote fits and black diagonal lines indicate the identity. Means and standard deviations of the differences (observed minus modeled) are summarized in Table 2.

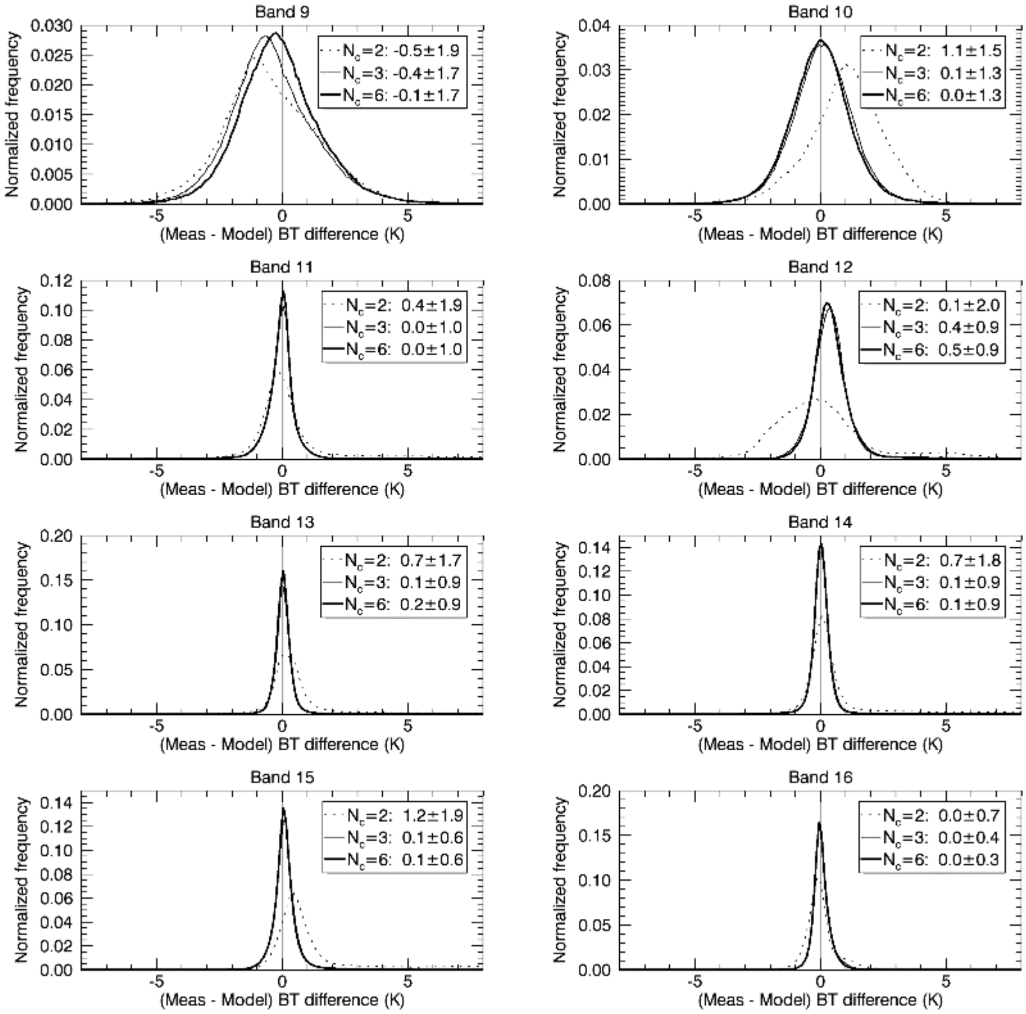

Fig. 4. Histograms of the brightness temperature (BT) differences between measurements and model calculations for the cloud retrieval results for full disk data of 12 UTC on August 20, 2015. Cloud retrieval was performed with CKD sets with different numbers of quadrature points (N_c). The means and standard deviations of the BT differences are shown in the legend in each panel.

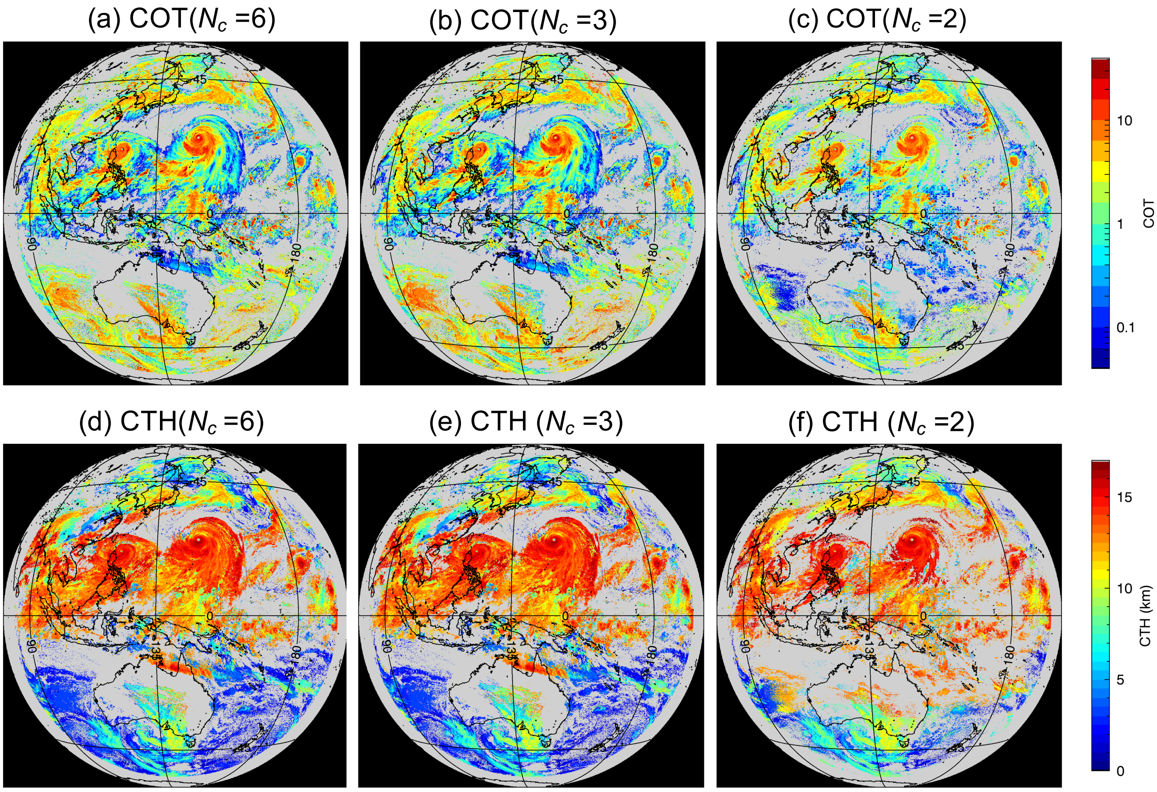

Fig. 5. Cloud optical thickness (COT) (a,b,c) and cloud top height (CTH) (d,e,f) retrieved by using CKD sets with different numbers of quadrature points (N_c) for full disk data at 12 UTC on 20 August 2015. Results are shown only for pixels with optimal solutions. (a,d) N_c = 6, (b,e) N_c = 3, and (c,f) N_c = 2.

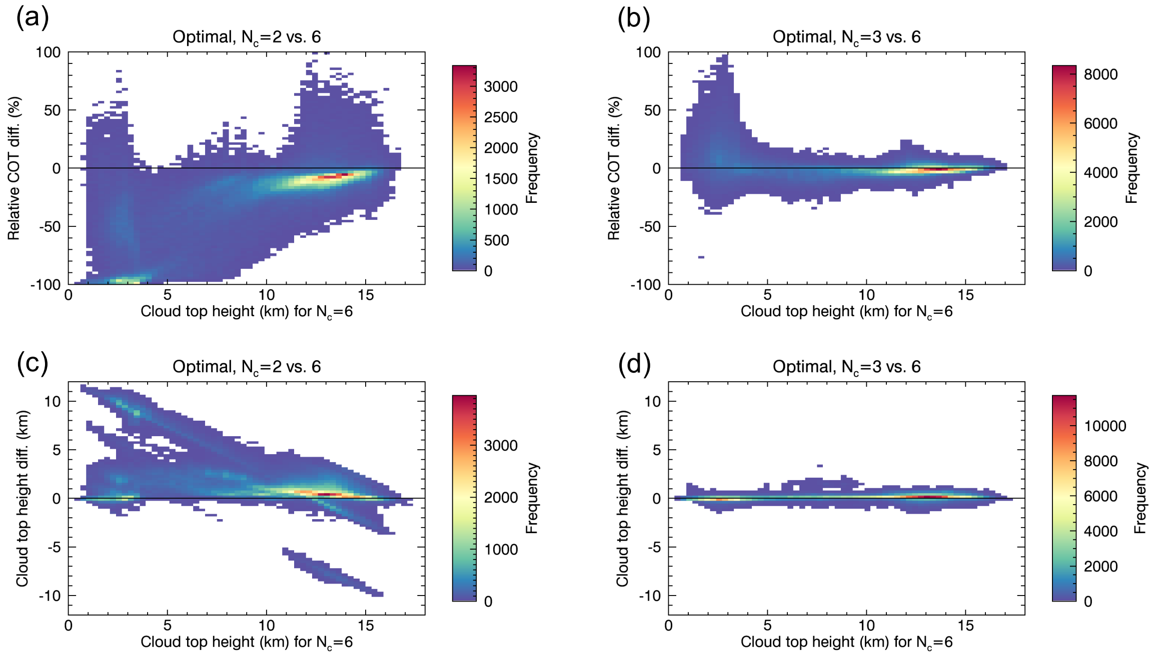

Fig. 6. Differences in (a,b) cloud optical thickness (COT) and (c,d) cloud top height (CTH) retrieved with CKD sets with different numbers of quadrature points. The vertical axes denote differences results with N_c = 2 (a,c) and N_c = 3 (b,d) from results with N_c = 6. The color shading denotes occurrence frequency. Results are shown only for optimal retrievals in both reduced (N_c = 2 or 3) and full (N_c = 6) sets.

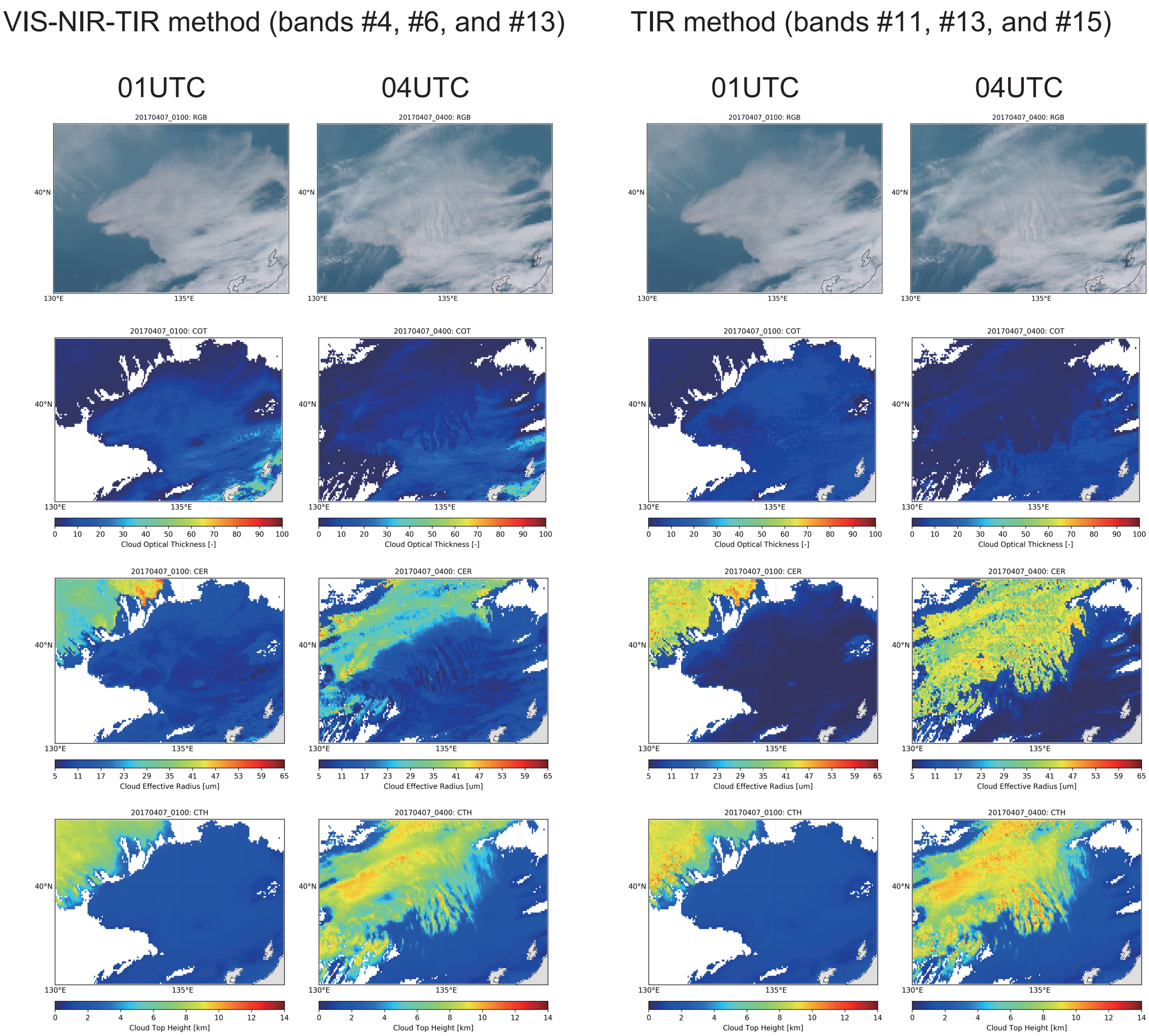

Figure 7. Sample of low clouds and overlapping cirrus clouds over the Sea of Japan at 01 and 04 UTC on 7 April 2017. Top, second, third, and bottom panels are true-color composite images and retrieved results of COT, CER, and CTH, respectively. The panels on the left were retrieved using VIS, NIR, and TIR bands (bands #4, #6, and #13, respectively). The panels on the right were retrieved using TIR bands (bands #11, #13 and #15) with a version of Rstar that was updated for this study.